Wavefield tomography using RTM backscattering

Esteban Díaz and Paul Sava
Center for Wave Phenomena, Colorado School of Mines, Golden CO 80401

ABSTRACT
Reverse time migration (RTM) backscattering contains kinematic information that can be used to constrain velocity models. The backscattering results from the correlation between forward scattered and backscattered wavefields from sharp interfaces, i.e. sediment-salt interfaces. The synchronization between these wavefields depends on the velocity of the sediment section and the correct interpretation of the sharp boundary. Therefore, we can use these events along with reflection and diving waves to define a joint optimization problem for velocity model building. As in RTM images, in gradient computation the backscattering and diving information produces cross-talk. In order to avoid the cross-talk, we use a directional filter based on the Poynting vector which preserves the components of the wavefield that travel in the same direction. Using backscattered waves for constraining the velocity in the sediment section requires defining the top of salt in advance, which would imply a dynamic workflow for model building in salt environments where both sediment velocity and salt interface change iteratively during inversion.

Key words: RTM backscattering, wavefield tomography, Poynting vector

1 INTRODUCTION

The two-way way equation is the engine of reverse-time migration (RTM) (Baysal et al., 1983; McMechan, 1983; Whitmore, 1983). This imaging technology is used routinely to obtain high fidelity images of the subsurface. Despite the computing cost, the two-way operator has many advantages over other modeling approaches, like downward continuation or Kirchhoff modeling. This technique is especially suited for complex geological settings such as those with strong velocity gradients, sharp boundaries (e.g. salt bodies), and strong lateral variations. The reason for the RTM success is that a wavefield reconstructed with the two-way operator can easily handle any dip, multi-pathing, and reflections from steep structures (Gray et al., 2001; Etgen et al., 2009).

RTM also produces low wave-number events in seismic images, which are usually referred to as RTM artifacts. The low wave-number energy is produced by the correlation of waves that propagate in the same direction, thus violating the assumptions of the conventional cross correlation imaging condition (Claerbout, 1985). Such events include backscattered waves, head-waves, and diving waves. The backscattered events obstruct the image representing the subsurface reflectivity, and so are usually considered noise. Numerous techniques can be employed to remove the RTM noise. In terms of filtering approach, we could divide such methods in two categories: pre-imaging filtering (Fletcher et al., 2005; Yoon et al., 2004; Liu et al., 2011) and post-imaging filtering (Youn and Zhou, 2001; Guitton et al., 2007; Zhang and Sum, 2009; Kaelin and Carvajal, 2011).

Although the low wavenumber energy is noise for imaging purposes, it can be used for velocity model-building. This energy is the result of the correlation of waves traveling in the same direction, thus coinciding in space and time. This space and time coincidence only occurs when the wavefields extrapolation is accurate. Therefore, if the velocity model is correct, the RTM backscattering is strong simply because the wavefields are synchronized (Díaz and Sava, 2012). For reflected data, the space-time synchronization criterion also applies at the reflector position. Since both types of waves (transmitted and reflected) share the same kinematic behaviour, we can design a joint optimization problem that improves the synchronization of all the data simultaneously,thus allowing us to refine the model and to use the RTM backscattering as a source of information instead of treating it as noise.

To optimize the velocity model, one can choose a method that is consistent with the modeling operator (two-way). Such an inverse problem could be formulated by finding a model that produces data which resembles the observed data, as is done in Full Waveform Inversion (Tarantola, 1984; Pratt, 1999). This data-domain approach relies on the kinematic and dynamic consistencies between modeled and observed data. Therefore, if the propagation engine used is not dynamically consistent with the data, i.e. the modeled amplitudes are not accurate, then the chances for convergence diminish. Alternatively, one can optimize the model in the image space using

techniques from the family usually referred to as wavefield tomography (Woodward, 1992; Sava and Biondi, 2004; Fliedner and Bevc, 2008; Shen and Symes, 2008; Yang and Sava, 2011a). The image domain approach seeks the kinematic synchronization of the wavefields at an image location. Therefore, the aim of this method is to improve the image focusing rather than to match the dynamic information of the wavefields as in done in the data-domain approach. This increases the robustness of the method, but decreases its ability to construct high resolution models. One way to formulate the problem in the image space is by using extended images (Rickett and Sava, 2002; Sava and Fomel, 2006; Sava and Vasconcelos, 2011), from which we can extract wavefield similarities in space and time (Shen et al., 2003; Yang and Sava, 2010). Extended images are normally used for optimizing the reflected data information, but Díaz and Sava (2012) show that similar to reflected data, the RTM backscattered energy also maps to zero time-lag and space-lag when the velocity model is correct.

In this paper, we demonstrate that it is possible to use the backscattered and diving waves for image-domain wavefield tomography. Using the two-way wave equation operator allows simultaneous inversion based on the reflected, diving and backscattered waves. We formulate the tomography problem using the adjoint state method (ASM), which is an efficient technique for gradient-based optimization (Plessix, 2006). However, the gradient computed using the ASM suffers from cross-talk between forward and backscattered waves, which produces undesirable reflector-like evens. In order to avoid the unwanted correlations, we apply a directional filter designed to keep the contributions between wavefields traveling in the same direction during the correlation step of the gradient computation. This filter is based on the Poynting vectors of the extrapolated wavefields (Yoon et al., 2004), although other filtering techniques can be used instead.

We start this paper with a brief review of the RTM backscattering kinematic properties and the mapping patterns in extended images, and then we review wavefield tomography using extended images. We show how this methodology can be adapted to backscattering energy and define an objective function and its gradient, which are essential for inversion. We then illustrate how we can make use of the backscattering information for wavefield tomography, and demonstrate our method using a complex synthetic based on the Sigsbee model (Paffenholz et al., 2002).

2 RTM BACKSCATTERING REVISITED

RTM backscattering is produced in the presence of sharp models, e.g. sediment-salt interfaces. In such cases, wavefields extrapolated with a two-way operator (e.g. the scalar wave equation)

$$\frac{1}{v^2(\mathbf{x})}\frac{\partial^2 u(\mathbf{x},t)}{\partial t^2} - \nabla^2 u(\mathbf{x},t) = f(\mathbf{x},t) \tag{1}$$

contains forward and backscattered components. Here, $u(\mathbf{x},t)$ the reconstructed wavefield, $v(\mathbf{x})$ the medium velocity and $f(\mathbf{x},t)$ the source function. Therefore, we can write the source wavefield as a superposition of two components

$$u_s(\mathbf{x},t) = u_s^b(\mathbf{x},t) + u_s^f(\mathbf{x},t), \tag{2}$$

where the superscripts ^{b} and ^{f} correspond to the backscattered and forward scattered wavefields from the sharp boundary, respectively. Similarly, the receiver wavefield can be decomposed into two components with the equivalent naming convention:

$$u_r(\mathbf{x},t) = u_r^b(\mathbf{x},t) + u_r^f(\mathbf{x},t). \tag{3}$$

2.1 Conventional imaging condition

The source and receiver wavefields allow one to construct an image with the conventional imaging condition (Claerbout, 1985) defined as the zero-lag correlation between source and receiver wavefields:

$$R(\mathbf{x}) = \sum_e \sum_t u_s(e,\mathbf{x},t) u_r(e,\mathbf{x},t). \tag{4}$$

Here e refers to the experiment index, e.g. shot number or plane-wave take-off angle.

If the wavefields used in imaging contain backscattering, we can substitute equations 2 and 3 into equation 4 and obtain an image which is a superposition of 4 individual images:

$$\begin{aligned} R(\mathbf{x}) = {} & R^{ff}(\mathbf{x}) + R^{bb}(\mathbf{x}) \\ & + R^{bf}(\mathbf{x}) + R^{fb}(\mathbf{x}). \end{aligned} \tag{5}$$

Following the convention in Díaz and Sava (2012), the first superscript corresponds to the source wavefield and the second to the receiver wavefield. In this total image, two components (^{ff} and ^{bb}) provide an estimate of the reflectivity, and the other two components (^{fb} and ^{bf}) represent backscattering. This means that the backscattering is produced from the correlation of wavefields traveling in the same direction. For example, $R^{bf}(\mathbf{x})$ is produced when the backscattered source wavefield $u_s^b(\mathbf{x},t)$ resembles the forward scattered receiver wavefield $u_r^f(\mathbf{x},t)$, and $R^{fb}(\mathbf{x})$ is produced with the opposite combination of the propagating wavefields. Several authors (Yoon et al., 2004; Fei et al., 2010; Liu et al., 2011) use this wavefield directionality notion to keep only the components related to reflectivity in the image and to remove everything else. Here we use the directionality concept to keep the components that travel in the same direction during tomography.

2.2 Extended imaging condition

A generalized version of equation 4 can be used to understand the (kinematic) similarities between source and receiver wavefields. This concept is known as extended imaging (Rickett and Sava, 2002; Sava and Fomel, 2006; Sava and Vasconcelos, 2011). A general case of an extended image is defined as follows:

$$R(\mathbf{x},\boldsymbol{\lambda},\tau) = \sum_e \sum_t u_s(e,\mathbf{x}-\boldsymbol{\lambda},t-\tau) u_r(e,\mathbf{x}+\boldsymbol{\lambda},t+\tau), \tag{6}$$

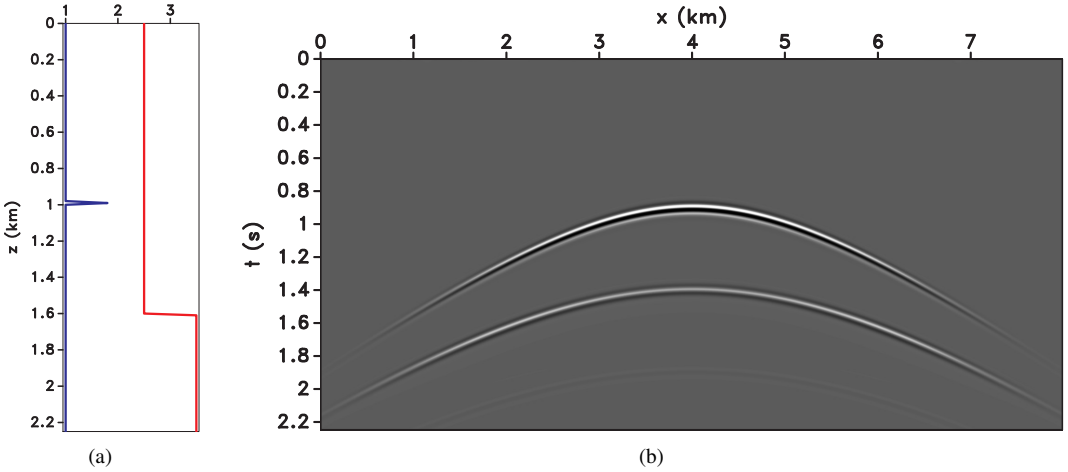

Figure 1. Synthetic experiment setup: (a) the density (spike function) model (g/cc) and the velocity (step function) model (km/s), and (b) the modeled data.

where $\boldsymbol{\lambda}$ and τ are space and time extensions of the cross-correlation, respectively. Extended images are commonly used to produce angle gathers (Sava and Fomel, 2003, 2006; Sava and Vlad, 2011) and for velocity estimation (Shen and Symes, 2008; Yang et al., 2012; Yang and Sava, 2011b).

In the presence of sharp models, we can substitute equations 2 and 3 into equation 6. By doing so, we can differentiate between the different components of the extended image, which is similar to what we do for conventional images:

$$R(\mathbf{x},\boldsymbol{\lambda},\tau) = R^{ff}(\mathbf{x},\boldsymbol{\lambda},\tau) + R^{bb}(\mathbf{x},\boldsymbol{\lambda},\tau) + R^{bf}(\mathbf{x},\boldsymbol{\lambda},\tau) + R^{fb}(\mathbf{x},\boldsymbol{\lambda},\tau). \quad (7)$$

The reflected data maps into the components ^{ff} and ^{bb}, whereas the backscattered energy maps into the ^{fb} and ^{bf} components. In the conventional image $R(\mathbf{x})$ (both backscattered and reflected energy) coexist above sharp interfaces, for example due to the presence of a salt body. The two components are usually separated based on the spectral content (the artifacts have low wavenumber content, whereas the reflectivity has high wavenumber content). This separation is normally done using some sort of high-pass filter, like a Laplacian (∇^2) operator (Youn and Zhou, 2001; Zhang and Sum, 2009) or by least-squares filtering (Guitton et al., 2007). The separation is not perfect in areas with similar spectral content. In the extended image space, however, the reflected and backscattered energy has unique mapping patterns (Díaz and Sava, 2012), which can be used to effectively separate both components (Kaelin and Carvajal, 2011).

Díaz and Sava (2012) show that the backscattered and reflected energy share the wavefield synchronization criterion. The spatial and temporal synchronization occurs above a sharp boundary for backscattered events, whereas the synchronization occurs at the position of the reflectors for reflected data. The synthetic model shown in Figure 1(a) illustrates the extended image kinematic sensitivity to model error. The data in Figure 1(b) show two events: the earlier one corresponding to a reflector in the density model (spike in Figure 1(a)), and the later one resulting from a sharp contrast in the velocity model (step function in Figure 1(a)). The third event in the data corresponds to an internal multiple generated between the density and velocity interfaces.

Figures 2(a), 2(b), and 2(c) show time-lag gathers for three different velocities. These gathers are generated using equation 6 with $\boldsymbol{\lambda} = \mathbf{0}$ after stacking over different experiments, i.e. shots in this case. We simulate a velocity error in the first layer and adjust the sharp boundary according to the migration velocity, for example a low velocity shifts the boundary upwards and a high velocity shifts the boundary downwards. The backscattering maps vertically in the three cases, however it deviates from $\tau = 0$ when the velocity is incorrect. The time delay error in the backscattering is the same to the one produced by the reflected energy at the sharp interface. Therefore, the backscattering provides information about the sharp interface at any place in the image above it.

Figures 3(a), 3(b), and 3(c) show the equivalent space-lag gather dependency with respect to the velocity error. Similar to the time-lag gathers, the space-lag gathers are generated after stacking the contribution from different experiments. The backscattering (mapping vertically in the gathers) spreads away from $\boldsymbol{\lambda} = \mathbf{0}$ with the velocity error, thus emulating the defocusing of the reflected data. Similarly to the time-lag gathers, the backscattering above the interface is the expression of the defocusing at the sharp boundary.

Since both reflected and backscattered data share similar velocity dependency, we conclude that we can design an inverse problem that optimizes both type of events simultaneously (Díaz and Sava, 2012). The following section details the velocity analysis procedure based on backscattering.

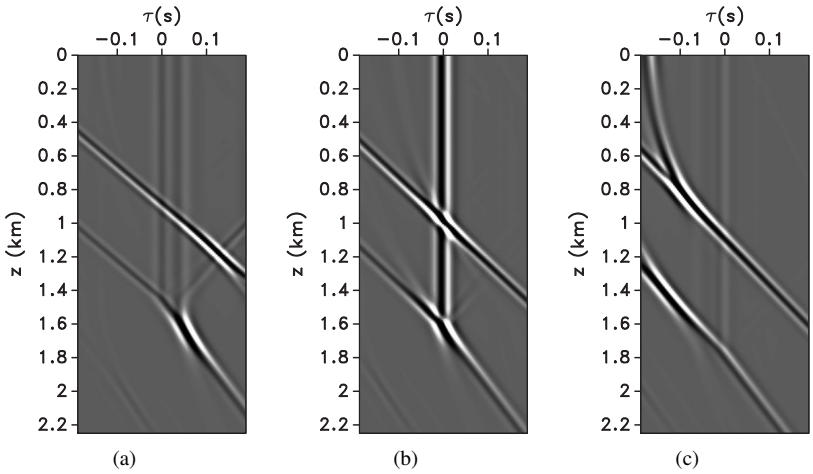

Figure 2. Time-lag gathers for (a) low, (b) correct and (c) high velocities.

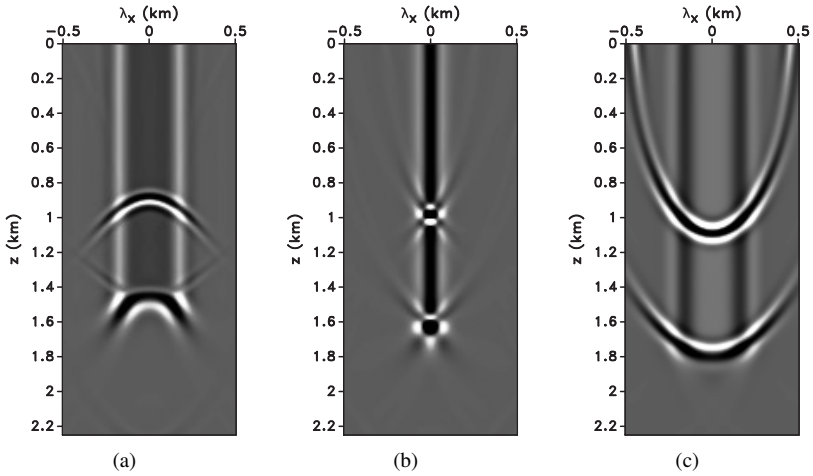

Figure 3. Space-lag gathers for (a) low, (b) correct and (c) high velocities.

3 WAVEFIELD TOMOGRAPHY WITH EXTENDED IMAGES

In order to analyze the velocity model error, we can make use of the semblance principle which seeks image consistency as a function of extended image parameters. Stork (1992) implements the idea using the consistency between common offset images. Symes and Carazzone (1991) exploit this concept using the differential semblance optimization (DSO) method. DSO can also be used to increase the flatness of angle gathers. Rickett and Sava (2002) and Sava and Fomel (2003) show that common angle gathers and extended images are related by a slant stacking operation. Therefore, these two type of common image gathers are equivalent for velocity analysis. Shen and Symes (2008) and Yang and Sava (2011a) use the consistency criterion in extended images to formulate a tomographic problem based on space-lag gathers or joint space and time-lag gathers, respectively.

3.1 Inversion with time-lag gathers

If the velocity is correct, the time-lag gathers (Sava and Fomel, 2006) show maximum focusing at zero lag. This observation derives from the fact that the source and receiver wavefields are synchronized at the reflector position. The velocity model can be improved by increasing the wavefield synchronization, which is equivalent to locating the events in the extended images as close as possible to $\tau = 0$. This can be done by minimizing the following objective function (OF):

$$J = \frac{1}{2} \left|\left| P(\tau) R(\mathbf{x}, \tau) \right|\right|^2 , \tag{8}$$

where $P(\tau) = |\tau|$ is an operator that penalizes the energy outside $\tau = 0$. Following the notation in Yang and Sava (2011a), we can express $R(\mathbf{x}, \tau)$ as

$$R(\mathbf{x}, \tau) = \sum_e \sum_t T(-\tau) u_s(e, \mathbf{x}, t) T(+\tau) u_r(e, \mathbf{x}, t), \tag{9}$$

where $T(\pm\tau)$ is a time-shift operator applied to the source or receiver wavefields. Note that this OF cannot drop to zero completely because in the time-lag gathers, there is always correlation energy for all values of τ. However, this OF is minimum when the velocity model is correct and most of the energy in the extended image locates at $\tau = 0$.

We compute the gradient of equation 8 using the Adjoint State Method (ASM) (Tarantola, 1984; Plessix, 2006). The adjoint source with respect to the source wavefield for an experiment e is

$$g_s(\mathbf{x}, e) = \sum_{\tau} T(-\tau)P^2(\tau)R(\mathbf{x}, \tau)T(-\tau)u_r(e, \mathbf{x}, t), \tag{10}$$

and the adjoint source with respect to the receiver wavefield is

$$g_r(\mathbf{x}, e) = \sum_{\tau} T(\tau)P^2(\tau)R(\mathbf{x}, \tau)T(\tau)u_s(e, \mathbf{x}, t). \tag{11}$$

We construct the adjoint state variables by injecting the adjoint sources at the gather positions and by extrapolating the wavefields using the adjoint modeling operators. The adjoint source wavefield $a_s(e, \mathbf{x}, t)$ is reconstructed backward in time, whereas the adjoint receiver wavefield $a_r(e, \mathbf{x}, t)$ is reconstructed forward in time. Using the state and adjoint state variables, the gradient with respect to the velocity model is

$$\nabla J(\mathbf{x}) = \frac{-2}{v^3(\mathbf{x})} \sum_e \sum_t \frac{\partial^2 u_s}{\partial t^2}(e, \mathbf{x}, t)a_s(e, \mathbf{x}, t) + \frac{\partial^2 u_r}{\partial t^2}(e, \mathbf{x}, t)a_r(e, \mathbf{x}, t), \tag{12}$$

where $\frac{-2}{v^3(\mathbf{x})}\frac{\partial^2}{\partial t^2}$ corresponds to the derivative of the modeling operator (equation 1) with respect to the velocity model.

In the gradient expression (equation 12) we expect to correlate state and adjoint state wavefields traveling in the same direction which implies that the gradient is smooth. However, if backscattering is present in the wavefield, we obtain cross-talk similar to that seen in RTM. The cross-talk in this case is generated by the correlation of wavefields traveling in the opposite direction. In order to attenuate the cross-talk, we can use a filter that preserves the components of wavefields traveling in the same direction and eliminates the wavefields traveling in opposite directions. We can find the direction of propagation using the approach of Yoon et al. (2004), which constructs the Poynting vectors $\mathbf{P}(e, \mathbf{x}, t)$ using the equation

$$\mathbf{P}(e, \mathbf{x}, t) \propto \frac{\partial u(e, \mathbf{x}, t)}{\partial t} \nabla u(e, \mathbf{x}, t), \tag{13}$$

where u can be either the source or the receiver wavefield. In practice we use the time-averaged Poynting vectors using a Gaussian smoothing over a small time window determined by the dominant period of the data

$$< \mathbf{P}(e, \mathbf{x}, t) >_t = \mathbf{P}(e, \mathbf{x}, t) * G(t). \tag{14}$$

Here, the symbol $*$ denotes convolution, and $G(t)$ is the Gaussian smoothing filter.

To keep just the wavefields components traveling in the same direction, we can compute a weighting function $W(\theta)$ with

$$\theta(\mathbf{x}, t) = \cos^{-1}\left(\frac{\mathbf{P}_s(\mathbf{x}, t) \cdot \mathbf{P}_r(\mathbf{x}, t)}{|\mathbf{P}_s(\mathbf{x}, t)||\mathbf{P}_r(\mathbf{x}, t)|}\right) \tag{15}$$

such that we preserve the wavefield cross-correlation for which $\mathbf{P}_s(\mathbf{x}, t) \cdot \mathbf{P}_r(\mathbf{x}, t) \approx 1$, i.e. when the direction of propagation is similar within a given tolerance. The weighting function can be designed using a cutoff angle, from which the function tapers off smoothly using a Gaussian function with standard deviation σ which defines the range from which the angles are accepted.

$$W(\theta, a, \sigma) = \begin{cases} 1 & : 0^\circ \leq \theta < a \\ e^{-(\theta-a)^2/(2\sigma^2)} & : a \leq \theta \leq 180^\circ. \end{cases} \tag{16}$$

Based on this filter, we change equation 12 to

$$\nabla J(\mathbf{x}) = \frac{-2}{v^3(\mathbf{x})} \sum_e \sum_t W(\theta)\frac{\partial^2 u_s}{\partial t^2}(e, \mathbf{x}, t)a_s(e, \mathbf{x}, t) + W(\theta)\frac{\partial^2 u_r}{\partial t^2}(e, \mathbf{x}, t)a_r(e, \mathbf{x}, t). \tag{17}$$

This new gradient avoids cross-talk and emphasizes wavefields traveling in the same direction.

Figures 4(a), 4(c), and 4(e) show the gradient constructed using equation 12 for low, correct, and high velocities, respectively. One can see that the intensity of the gradient with correct velocity is lower that obtained for either low or high velocities. One can also observe the cross-talk due to wavefields propagating in opposite directions which appears as reflectors in the gradient. The gradient is computed using equation 17 with a cutoff angle $a = 15^\circ$, Figures 4(b), 4(d), and 4(f) show the cross-talk significantly attenuated.

3.2 Inversion with space-lag gathers

We can also use the information contained in space-lag gathers (Rickett and Sava, 2002). If the velocity model is correct, then space-lag gathers focus at $\boldsymbol{\lambda} = \mathbf{0}$. If the velocity model is incorrect, the gathers contain defocused energy outside $\boldsymbol{\lambda} = \mathbf{0}$. This criterion is used by Shen and Symes (2008) and Yang and Sava (2011a) to formulate wavefield tomography using the OF

$$J = \frac{1}{2}\left|\left|P(\boldsymbol{\lambda})R(\mathbf{x}, \boldsymbol{\lambda})\right|\right|^2, \tag{18}$$

where $P(\boldsymbol{\lambda}) = |\boldsymbol{\lambda}|$ is a penalty operator. Even with correct velocity, this OF does not become zero due to the band-limited nature of the data and due to illumination effects (Yang et al., 2012). Nevertheless, this OF provides an effective criterion for velocity updating.

We compute the gradient of equation 18 using the same workflow as the one used for equation 8 (Yang and Sava, 2011a). The adjoint sources are defined as

$$g_s(\mathbf{x}, e) = \sum_{\boldsymbol{\lambda}} T(-\boldsymbol{\lambda})P^2(\boldsymbol{\lambda})R(\mathbf{x}, \boldsymbol{\lambda})T(-\boldsymbol{\lambda})u_r(e, \mathbf{x}, t) \tag{19}$$

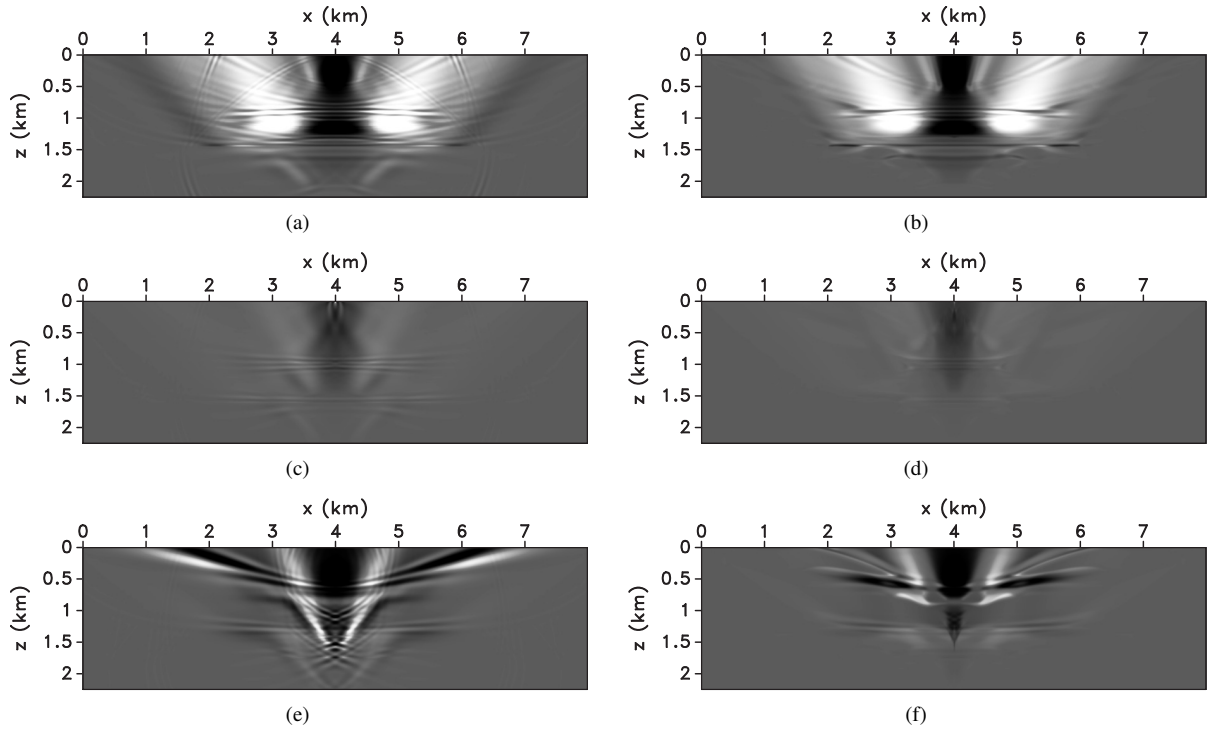

Figure 4. Gradients obtained using time-lag gathers for (a)-(b) low, (c)-(d) correct, and (e)-(f) high velocities. Gradients (a), (c), and (e) are constructed without filtering and (b), (d) and (f) with filtering.

for the source side, and

$$g_r(\mathbf{x}, e) = \sum_{\boldsymbol{\lambda}} T(+\boldsymbol{\lambda}) P^2(\boldsymbol{\lambda}) R(\mathbf{x}, \boldsymbol{\lambda}) T(+\boldsymbol{\lambda}) u_s(e, \mathbf{x}, t) \tag{20}$$

for the receiver side. Here $T(\pm\boldsymbol{\lambda})$ is a space shifting operator applied to the wavefields. The only difference between the time-lag and space-lag gather formulation is in the OF and in the computation of the adjoint sources. The gradient and adjoint wavefields are computed using the same wave-equation and background velocity model as in the case of thetime-lag gathers (equations 12 and 17).

Figures 5(a), 5(c), and 5(e) show the gradients for low, correct, and high velocity, respectively. To compute these gradients, we use the space-lag gathers shown in Figures 3(a), 3(b), and 3(c), respectively. As for the gradient constructed with time-lag gather, one can see that the energy in the space-lag gradient is proportional to the focusing error observed in the gathers. The gradients obtained using equation 12 also contain cross-talk similarly to the gradient constructed with time-lag gathers. If we apply the directional filtering during the gradient computation (equation 17), we obtain gradients with significantly lower cross-talk. Figures 5(b), 5(d), and 5(f) show the filtered gradients for the low, correct, and high velocity models, respectively.

4 EXAMPLES

In this section, we illustrate the use of the backscattering and reflected events on a modified version of the Sigsbee 2b model (Paffenholz et al., 2002). We focus on the small basin formed by the salt intrusion (Figure 6(a)). We simulate data for 61 shots evenly distributed on the surface, with a fixed receiver array at the surface, in order to test the effect of using a fast sediment velocity with an error increasing with depth (Figure 6(b)). After migrating the data with the fast sediment velocity, we interpret the top of salt (TOS) and place the salt bellow it as shown in Figure 6(c). Figure 6(d) shows the difference between Figure 6(c) and Figure 6(a), and indicates that overall the incorrect velocity is faster.

Figure 7(a) depicts the RTM image using the velocity in Figure 6(b), and show that the focusing of the TOS event degrades with depth and is not simple to interpret. Figure 7(b) shows evenly sampled space-lag gathers, which also indicate that the defocusing increases with depth. Figure 7(a) shows the RTM image obtained with the model after salt flooding (Figure 6(c)). One can see that the backscattering above the TOS event is not uniform and changes sign throughout the sediment section, thus indicating velocity or TOS interpretation error. Figure 7(b) shows space-lag gathers corresponding to the RTM image in Figure 7(c). Note that the backscattering (mapping vertically in the gathers) spreads away from $\boldsymbol{\lambda} = \mathbf{0}$, following the defocusing of the TOS reflector.

Figure 8(a) shows the gradient computed using the ve-

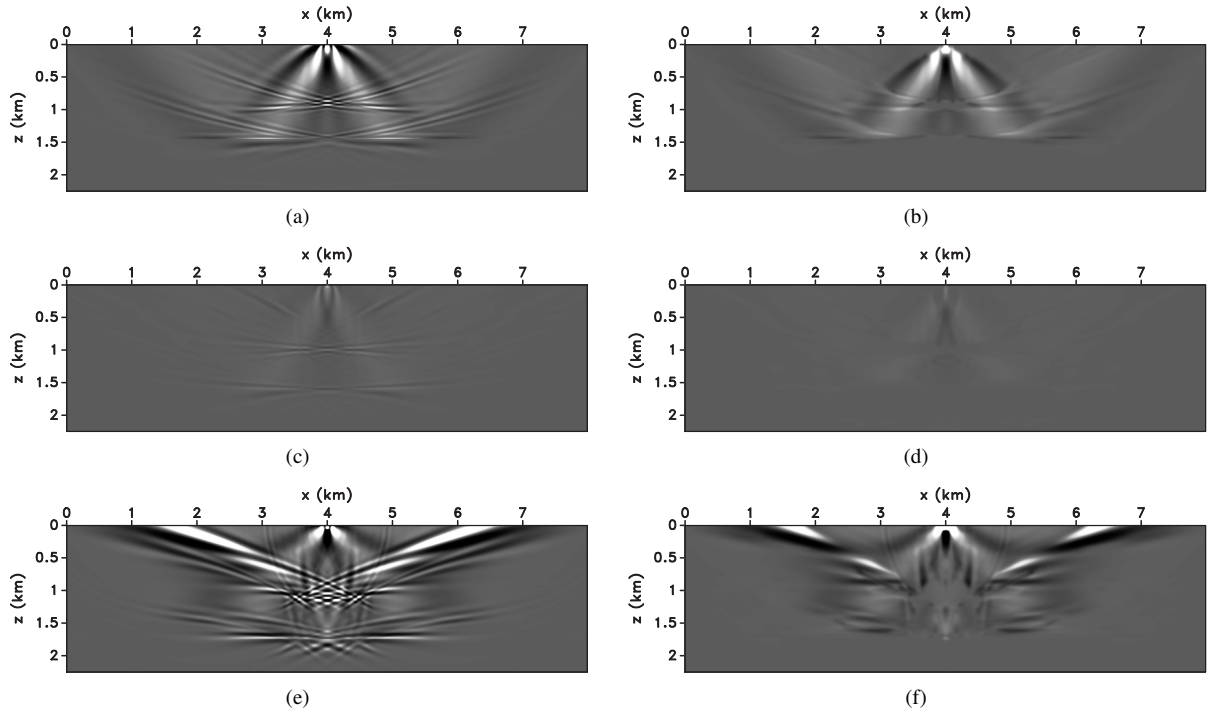

Figure 5. Gradients obtained using space-lag gathers for (a)-(b) low, (c)-(d) correct, and (e)-(f) high velocities. Gradients (a), (c), and (e) are constructed without filtering and (b), (d) and (f) with filtering.

locity in Figure 6(c). Figure 8(b) shows the filtered gradient, whereas Figure 8(c) shows the difference between the gradients in Figures 8(a)-8(b). One can see that the gradient energy is concentrated above the sharp boundary; therefore the update is correctly focused in the sediment basin, and the cross-talk is effectively removed by our filter using the Poynting vectors.

Since we use the top of salt for the tomography update, it is necessary to interpret the TOS event at each iteration. Interpretation of salt boundaries could be very difficult and time consuming, especially in complicated salt bodies with overhanging flanks (Ahmed et al., 2012). Since the sediment velocity changes at each iteration, the TOS also changes slowly with iteration. In practice, one could interpret the salt boundary in the first iteration and look for TOS changes in the vicinity of the previous solution, for example using automatic salt interpretation (Lomask et al., 2007; Halpert, 2011).

For comparison, we also compute a gradient using the fast sediment velocity shown in Figure 6(b) and the corresponding space-lag gathers in Figure 7(b). The gradient depicted in Figure 9(a) shows that some cross-talk is still present, despite the fact that strong sharp boundaries are not present in the model. We hypothesize that the cross-talk in the gradient is due to diving waves in the wavefields. The filtered gradient shown in Figure 9(a) and the difference shown in Figure 9(b) indicate that the filter effectively removes the cross-talk.

5 CONCLUSIONS

We demonstrate that it is possible to use RTM backscattered data in wavefield tomography. The RTM backscattering provides information about the wavefield synchronization and focusing of the sharp boundaries at any place in the image above the boundaries. As for RTM imaging, sharp models introduce cross-talk in wavefield tomography gradients, which appears as reflections instead of low wavenumber events as in the case of RTM images. We filter the cross-talk with an approach based on Poynting vectors to emphasise the wavefield components traveling in the same direction and to discard the wavefield components traveling in opposite directions. The purpose of this filter is exactly the opposite of the one proposed by Yoon et al. (2004) to attenuate the backscattering energy in RTM images.

We can use the backscattered information and sharp boundaries in the model to constrain the sediment velocity in the upper section. Using this information requires a dynamic model building work flow, with both the sediment and salt boundaries being updated at every iteration. Although we demonstrate the presence of cross-talk with extended images wavefield tomography, we assert that similar events exist in other two-way domain tomography methods, e.g. waveform inversion. Nevertheless, we conclude that sharp sediment-salt interfaces generate information useful for model updates.

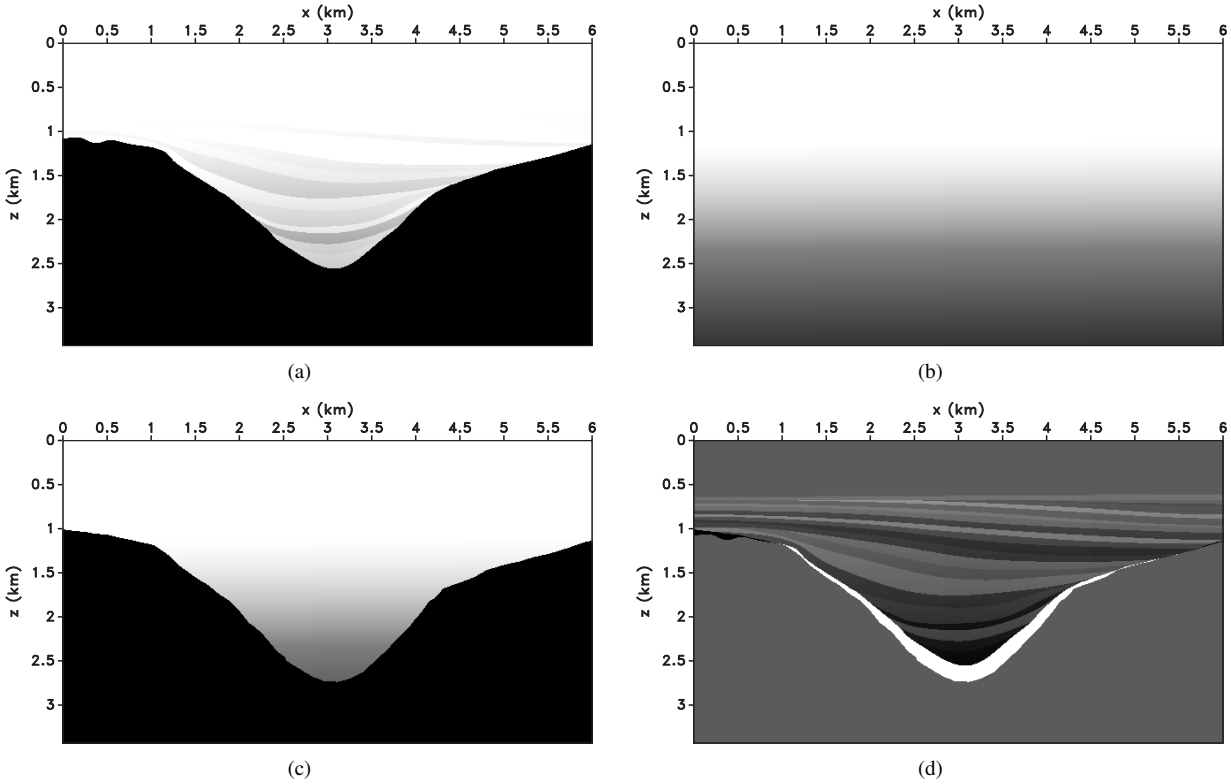

Figure 6. Salt model example: (a) true velocity model, (b) fast sediment flood velocity model, (c) fast sediment velocity with salt flood, and (c) the difference (c)-(a). In the difference, dark colors indicate positive difference and light colors indicate negative differences

6 ACKNOWLEDGMENTS

We would like to thank the sponsor companies of the Consortium Project on Seismic Inverse Methods for Complex Structures. The reproducible numeric examples in this paper use the Madagascar open-source software, freely available from http://www.ahay.org. We thank SMAART JV for the synthetic model. Esteban Díaz would like to thank to Natalya Patrikeeva and Tongning Yang for stimulating discussions about the Poynting vector and wavefield tomography, respectively.

REFERENCES

Ahmed, I., R. Faerber, C. Kumar, and F. Billette, 2012, Interactive velocity model validation (IVMV): SEG Technical Program Expanded Abstracts 2012, 1–5.

Baysal, E., D. D. Kosloff, and J. W. C. Sherwood, 1983, Reverse time migration: Geophysics, **48**, 1514–1524.

Claerbout, J. F., 1985, Imaging the earth's interior: Blackwell Scientific Publications, Inc.

Díaz, E., and P. Sava, 2012, Understanding the reverse time migration backscattering: noise or signal?: SEG Technical Program Expanded Abstracts 2012, 1–6.

Etgen, J., S. Gray, and Y. Zhang, 2009, An overview of depth imaging in exploration geophysics: Geophysics, **74**, WCA5–WCA17.

Fei, T. W., Y. Luo, and G. T. Schuster, 2010, De-blending reverse-time migration: SEG Technical Program Expanded Abstracts, **29**, 3130–3134.

Fletcher, R. F., P. Fowler, P. Kitchenside, and U. Albertin, 2005, Suppressing artifacts in prestack reverse time migration: SEG Technical Program Expanded Abstracts, **24**, 2049–2051.

Fliedner, M., and D. Bevc, 2008, Automated velocity model building with wavepath tomography: Geophysics, **73**, VE195–VE204.

Gray, S., J. Etgen, J. Dellinger, and D. Whitmore, 2001, Seismic migration problems and solutions: Geophysics, **66**, 1622–1640.

Guitton, A., B. Kaelin, and B. Biondi, 2007, Least-squares attenuation of reverse-time-migration artifacts: Geophysics, **72**, S19–S23.

Halpert, A. D., 2011, Model-building with image segmentation and fast image updates: 4035–4039.

Kaelin, B., and C. Carvajal, 2011, Eliminating imaging artifacts in RTM using pre-stack gathers: SEG Technical Program Expanded Abstracts, **30**, 3125–3129.

Liu, F., G. Zhang, S. A. Morton, and J. P. Leveille, 2011, An effective imaging condition for reverse-time migration using wavefield decomposition: Geophysics, **76**, S29–S39.

Lomask, J., R. Clapp, and B. Biondi, 2007, Application of image segmentation to tracking 3d salt boundaries: Geo-

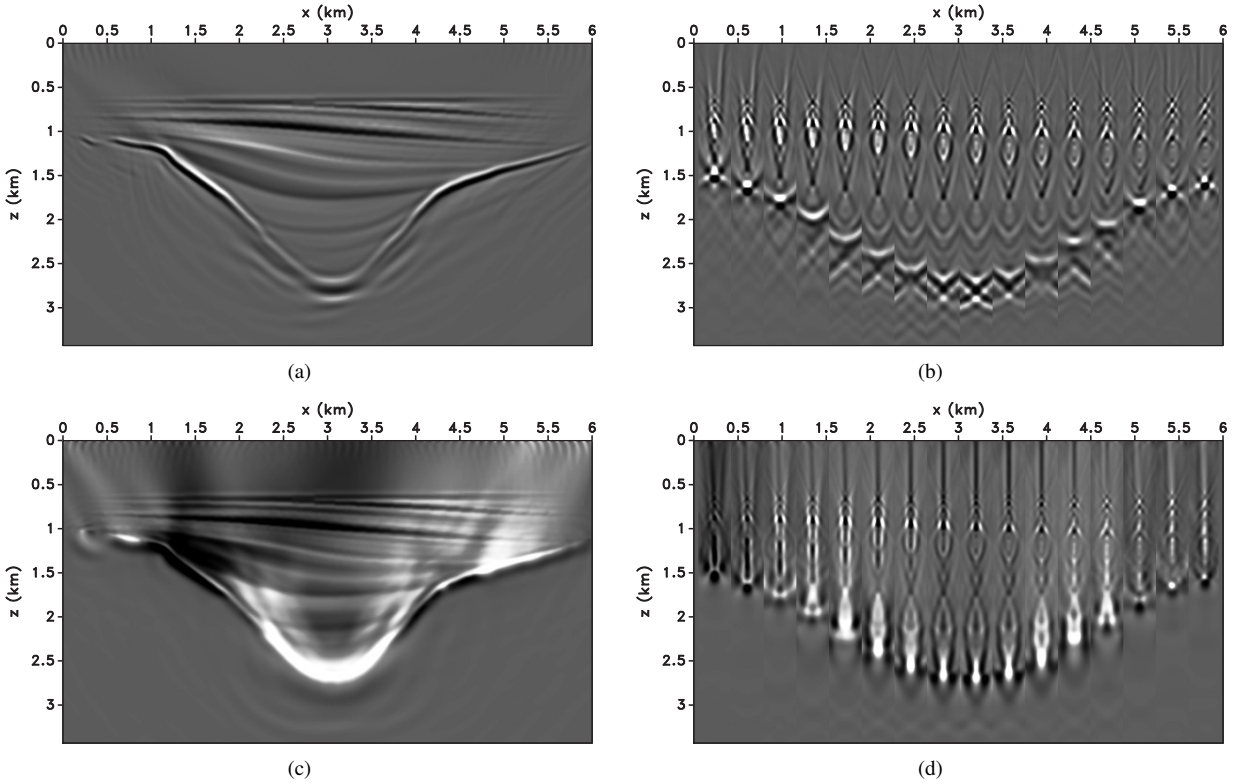

Figure 7. Imaging experiments using different velocities: (a) RTM and (b) space-lag gathers using fast sediment velocity from Figure 6(b), (c) RTM and (d) space-lag gathers using fast sediment velocity with salt flood from Figure 6(c).

physics, **72**, P47–P56.

McMechan, G. A., 1983, Migration by extrapolation of time-dependent boundary values: Geophysical Prospecting, **31**, 413–420.

Paffenholz, J., B. McLain, J. Zaske, and P. Keliher, 2002, Subsalt multiple attenuation and imaging: Observations from the Sigsbee 2B synthetic dataset: 72nd Annual International Meeting, SEG, Expanded Abstracts, 2122–2125.

Plessix, R.-E., 2006, A review of the adjoint-state method for computing the gradient of a functional with geophysical applications: Geophysical Journal International, **167**, 495–503.

Pratt, R. G., 1999, Seismic waveform inversion in the frequency domain, Part I: Theory and verification in a physical scale model: Geophysics, **64**, 888–901.

Rickett, J. E., and P. C. Sava, 2002, Offset and angle-domain common image-point gathers for shot-profile migration: Geophysics, **67**, 883–889.

Sava, P., and B. Biondi, 2004, Wave-equation migration velocity analysis - I: Theory: Geophysical Prospecting, **52**, 593–606.

Sava, P., and S. Fomel, 2006, Time-shift imaging condition in seismic migration: Geophysics, **71**, S209–S217.

Sava, P., and I. Vasconcelos, 2011, Extended imaging conditions for wave-equation migration: Geophysical Prospecting, **59**, 35–55.

Sava, P., and I. Vlad, 2011, Wide-azimuth angle gathers for wave-equation migration: Geophysics, **76**, S131–S141.

Sava, P. C., and S. Fomel, 2003, Angle-domain common-image gathers by wavefield continuation methods: Geophysics, **68**, 1065–1074.

Shen, P., and W. W. Symes, 2008, Automatic velocity analysis via shot profile migration: Geophysics, **73**, VE49–VE59.

Shen, P., W. W. Symes, and C. C. Stolk, 2003, Differential semblance velocity analysis by wave-equation migration: SEG Technical Program Expanded Abstracts, **22**, 2132–2135.

Stork, C., 1992, Reflection tomography in the postmigrated domain: Geophysics, **57**, 680–692.

Symes, W., and J. Carazzone, 1991, Velocity inversion by differential semblance optimization: Geophysics, **56**, 654–663.

Tarantola, A., 1984, Inversion of seismic reflection data in the acoustic approximation: Geophysics, **49**, 1259–1266.

Whitmore, N. D., 1983, Iterative depth migration by backward time propagation: SEG Technical Program Expanded Abstracts, **2**, 382–385.

Woodward, M., 1992, Wave-equation tomography: Geophysics, **57**, 15–26.

Yang, T., and P. Sava, 2010, Moveout analysis of wave-equation extended images: Geophysics, **75**, 151–161.

———, 2011a, Image-domain waveform tomography with

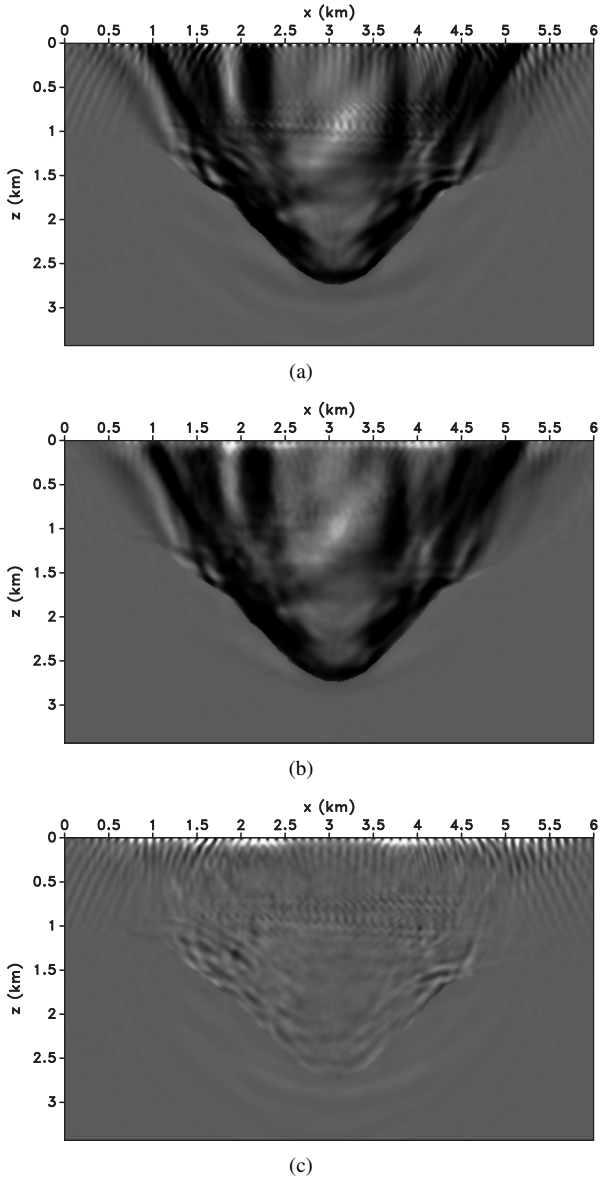

Figure 8. Gradients for salt model example using velocity in Figure 6(c): (a) gradient without filter, (b) gradient with directional filter, and (c) the difference.

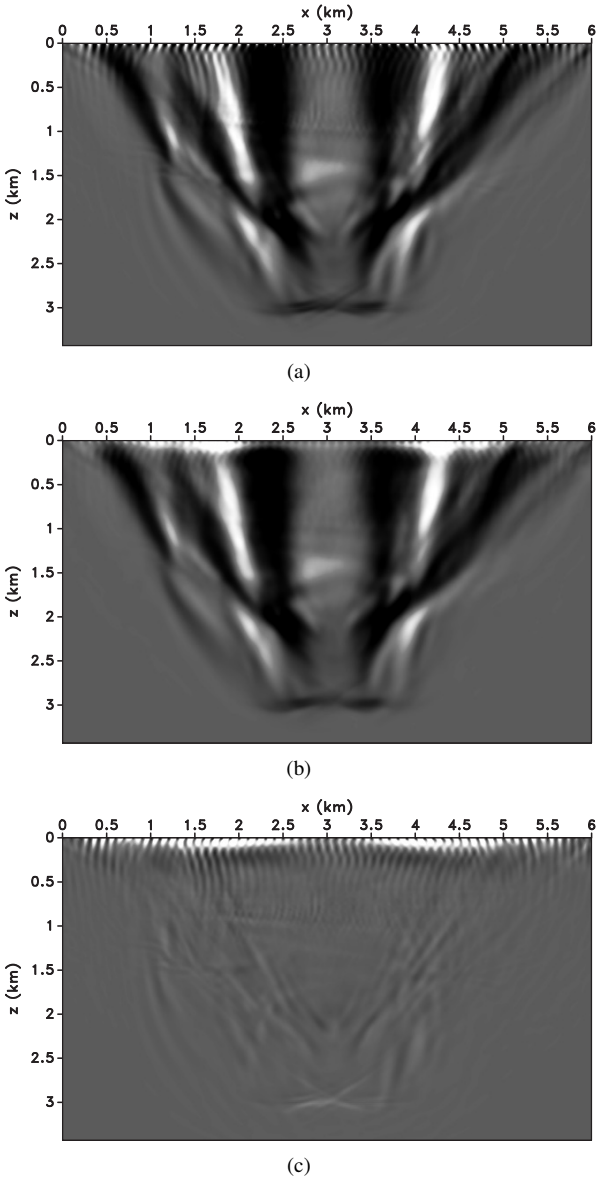

Figure 9. Gradients for salt model example using velocity in Figure 6(b): (a) gradient without filter, (b) gradient with directional filter, and (c) the difference.

two-way wave-equation: SEG Technical Program Expanded Abstracts 2011, **508**, 2591–2596.

———, 2011b, Wave-equation migration velocity analysis with time-shift imaging: Geophysical Prospecting, **59**, 635–650.

Yang, T., J. Shragge, and P. C. Sava, 2012, Illumination compensation for image-domain wavefield tomography: Submitted to Geophysics.

Yoon, K., K. J. Marfurt, and W. Starr, 2004, Challenges in reversetime migration: SEG Technical Program Expanded Abstracts, 1057–1060.

Youn, O. K., and H. Zhou, 2001, Depth imaging with multiples: Geophysics, **66**, 246–255.

Zhang, Y., and J. Sum, 2009, Practical issues in reverse time migration: true amplitude gathers, noise removal and harmonic source encoding: First Break, **27**, 53–59.